International Journal of Mass Spectrometry 434 (2018) 7–16

Contents lists available at ScienceDirect

International Journal of Mass Spectrometry

journal homepage: www.elsevier.com/locate/ijms

Full Length Article

Di-niobium gold clusters: Multiply-bonded Nb_2 dimer coordinated equatorially by Au atoms

Tian Jian, Ling Fung Cheung, Teng-Teng Chen, Gary V. Lopez, Wei-Li Li, Lai-Sheng Wang*

Department of Chemistry, Brown University, Providence, RI 02912, USA

ARTICLE INFO

Article history:
Received 20 June 2018
Received in revised form 23 July 2018
Accepted 31 August 2018
Available online 8 September 2018

Keywords:
Photoelectron spectroscopy
Bimetallic clusters
Gold
Niobium
Metal-metal bonding

ABSTRACT

We report a joint experimental and theoretical investigation on the structures and bonding of a series of di-niobium gold clusters, $Nb_2Au_x^-$ (x = 2–5), using photoelectron spectroscopy and density functional calculations. Well-resolved spectral features are observed for the $Nb_2Au_x^-$ clusters at different photon energies. Global minimum searches coupled with density functional calculations are performed to find the low-lying structures of the bimetallic clusters. Vertical detachment energies are calculated and compared with the experimental spectra to determine the global minimum structures. The $Nb_2Au_x^-$ (x = 2–5) clusters are found to feature a multiply-bonded Nb_2 dimer coordinated equatorially by the Au atoms with D_{xh} symmetries for x = 2–5, respectively. Each Au atom interacts with the Nb_2 dimer via a 3-center delocalized σ bond, while there are no Au. . .Au interactions. The Nb—Nb bond length is found to increase as the number of gold atoms increases in the $Nb_2Au_x^-$ (x = 2–5) clusters, as a result of the decrease of the bond order for the Nb_2 moiety from x = 2 to 5.

© 2018 Elsevier B.V. All rights reserved.

1. Introduction

The relativistic effects stabilize the 6*s* orbital of gold, while destabilizing its 5*d* orbitals, resulting in a reduced 5*d*-6*s* gap and significant *s*-*d* hybridization [1]. The strong relativistic effects bestow many unusual chemical and physical properties to gold [2–5], including its iconic golden color and its chemical inertness. The stabilization of the 6*s* orbital gives rise to both a unusually large ionization energy and a large electron affinity for the Au atom. The eletronegativity of Au (2.54 on the Pauling scale) is higher than that of the H atom (2.20) and comparable to that of the Se atom (2.55). Hence, Au can even act as an electron acceptor to form ionic compounds with alkali metals [6,7]. One of the most remarkable chemical properties of Au is its tendency to form covalent bonds [8–10]. In fact, it has been shown that Au can behave like H in its bonding to main-group elements in binary Au clusters with strong M–Au covalent bonds [11–34]. Transition metal doped gold clusters display a wide range of interesting structural features, ranging from halide-like structures in MAu_4 type clusters to planar $M@Au_6$ type structures and 3D structures [35–46].

Recently, the $Nb_2Au_6^-$ bimetallic cluster was found to be a highly symmetric D_{6h} molecular wheel, which contains an extremely short Nb≡Nb triple bond coordinated equatorially by an Au_6 ring [47]. The Au_6 ring is bonded by three delocalized σ bonds and interacts with the Nb_2 moiety via two 8-center-2-electron (8c-2e) delocalized bonds of *d*-*d* characters. This was a surprising observation and was in contrast to the D_{6h} Nb_2B_6 cluster [48], which features a B_6 ring sandwiched by two Nb atoms without significant Nb. . .Nb bonding. Clearly, there is a competition between Nb—Nb bonding and Nb—M bonding in the Nb_2M_6 type of clusters.

In the current work, we study a series of di-niobium-doped gold clusters $Nb_2Au_x^-$ (x = 2–5), using photoelectron spectroscopy (PES) and density functional theory (DFT) calculations, to help understand the growth of the bimetallic clusters and the formation of the $Nb_2Au_6^-$ molecular wheel. We find that Au atoms nucleate around a multiply-bonded Nb_2 dimer equatorially forming highly symmetric D_{xh} type structures for x = 2–5, on their way to D_{6h} in $Nb_2Au_6^-$. Notably, there is no Au—Au interaction between the equatorial Au atoms from x = 2 to 5, because of the large Au—Au separations and the strong Au—Nb bonding. Each Au atom is coordinated to the Nb_2 dimer via a 3-center σ bond, in contrast to $Nb_2Au_6^-$, in which the six Au atoms form a perfect ring with strong delocalized σ bonding around a triply-boned Nb≡Nb moiety.

2. Experimental and theoretical methods

2.1. Photoelectron spectroscopy

The experiments were carried out using a magnetic-bottle PES apparatus equipped with a laser vaporization supersonic cluster

* Corresponding author.
E-mail address: Lai-Sheng_Wang@brown.edu (L.-S. Wang).

https://doi.org/10.1016/j.ijms.2018.08.013
1387-3806/© 2018 Elsevier B.V. All rights reserved.

source, details of which have been published elsewhere [49,50]. The second harmonic radiation (532 nm) from a Nd:YAG laser was used to ablate a mixed target made of niobium and gold powder. A helium carrier gas seeded with 5% argon was used to quench the laser-induced plasma and initiate nucleation and cluster formation. Clusters formed in the nozzle were entrained in the carrier gas and underwent a supersonic expansion. Negatively charged clusters were extracted from the collimated cluster beam and analyzed by a time-of-flight mass spectrometer. The $Nb_2Au_x^-$ (x = 2–5) clusters of interest were mass-selected, decelerated and photodetached in the interaction zone of the magnetic-bottle electron analyzer. Several detachment laser photon energies were used, including the 193 nm (6.424 eV) radiation from an ArF excimer laser, and 266 nm (4.661 eV), 355 nm (3.496 eV), or 532 nm (2.331 eV) from a Nd:YAG laser. Photoelectrons were collected at nearly 100% efficiency and analyzed in a 3.5-meter-long electron flight tube. The photoelectron spectra were calibrated by the known spectra of Au^- or Bi^-. The energy resolution of the apparatus was $\Delta E_k/E_k \approx 2.5\%$, i.e., ~25 meV for electrons with 1 eV kinetic energy.

2.2. Theoretical methods

Global minima were searched for $Nb_2Au_x^-$ (x = 2–5) employing the simulated annealing algorithm [51,52] coupled with DFT structure optimization. In the initial searches at the PW91 level [53], the Los Alamos basis set and effective core potential (LANL2DZ) [54] were applied to both the Au and Nb atoms. Low-lying isomers from the initial searches were further re-optimized using the PW91 and PBE0 [55,56] functional with the Def2-TZVPPD [57,58] basis set and the Stuttgart-Dresden (SDD) [59,60] relativistic effective core potential (ECP28MDF for Nb and ECP60MDF for Au). Vibrational frequency calculations were done to verify that the low-lying isomers found were true energy minima on the potential energy surface. Vertical detachment energies (VDEs) were calculated using the PW91 functional, which was shown previously to be excellent for transition metal doped gold clusters [39]. The first VDE was calculated as the energy difference between the neutral and the anion at the optimized geometry of the anion, while higher VDEs were obtained using the time-dependent DFT (TD-DFT) [61] calculations of the neutrals. The vertical excitation energies of the neutral at the anion geometry were added to the first VDE to approximate the higher VDEs. The computed VDEs were fitted with unit-area Gaussian functions of 0.03 eV width to obtain the simulated spectra, which were used qualitatively to compare with the experimental PE spectra. Chemical bonding analyses were done using the adaptive natural density partitioning (AdNDP) [62,63] method at the PW91/Def2-TZVPPD level of theory. The structural and chemical bonding pictures were visualized using GaussView 4.1 [64]. All the calculations were carried out using Gaussian 09 [65].

3. Experimental results

The photoelectron spectra of $Nb_2Au_x^-$ (x = 2–5) at different photon energies are shown in Figs. 1–4, respectively. The detachment transitions are labeled as X, A, B. . ., which denote the transitions from the ground electronic state of the anion to the ground and excited electronic states of the neutrals, respectively. The VDEs of the resolved bands are measured from the peak maxima, as given in Table 1 for the four bimetallic clusters.

The 532 nm spectrum of $Nb_2Au_2^-$ (Fig. 1a) shows two sharp peaks. The intense peak X has a VDE of 1.82 eV, and the weak peak A has a VDE of 1.97 eV. At 355 nm (Fig. 1b), four more bands (B, C, D and E) are observed following a small energy gap from band A. Bands B and C are sharper, while D and E are quite broad. Bands D and E are better defined in the 266 nm and 193 nm spectra,

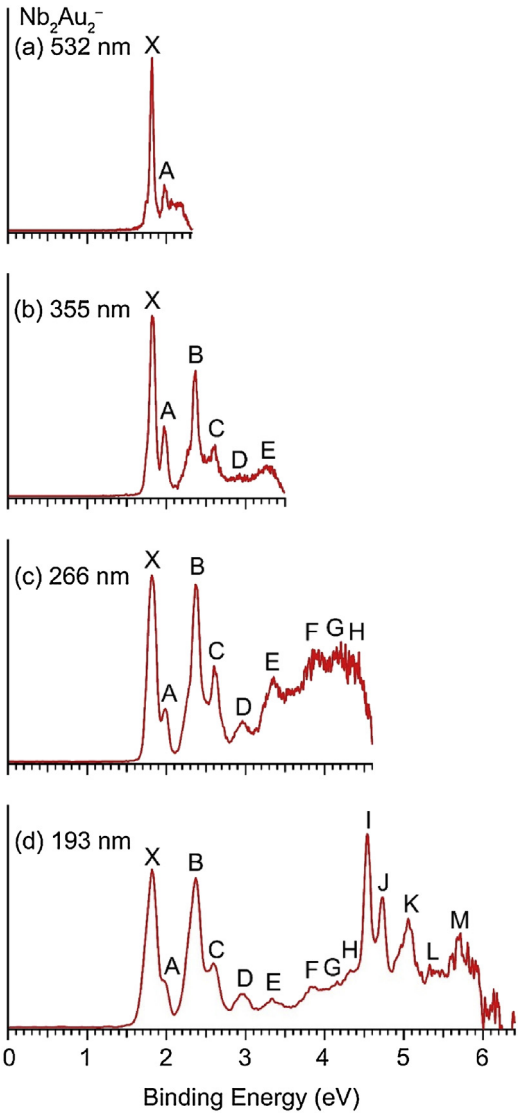

Fig. 1. Photoelectron spectra of $Nb_2Au_2^-$ at (a) 532 nm, (b) 355 nm, (c) 266 nm, and (d) 193 nm.

Table 1
Observed VDEs from the photoelectron spectra of the $Nb_2Au_x^-$ (x = 2 – 5) clusters. All energies are in eV[a].

$Nb_2Au_2^-$	VDE	$Nb_2Au_3^-$	VDE	$Nb_2Au_4^-$	VDE	$Nb_2Au_5^-$	VDE
X	1.82(2)	X'	1.81(2)	X	2.29(3)	X	2.86(3)
A	1.97(2)	X	1.96(2)	A	2.87(3)	A	3.19(3)
B	2.37(3)	A	2.60(3)	B	3.13(3)	B	3.60(3)
C	2.60(4)	B	2.82(3)	C	3.32(3)	C	4.68(4)
D	2.96(5)	C	3.23(4)	D	3.92(6)	D	4.93(5)
E	3.35(5)	D	3.69(4)	E	4.60(5)	E	~5.5
F	3.84(5)	E	5.08(5)	F	4.92(5)	F	~5.7
G	4.15(5)	F	5.61(5)	G	5.68(6)	G	~6.1
H	4.31(5)			H	6.09(6)		
I	4.55(5)						
J	4.73(5)						
K	5.06(6)						
L	5.33(7)						
M	5.71(7)						

[a] Numbers in parentheses represent the uncertainty in the last digit.

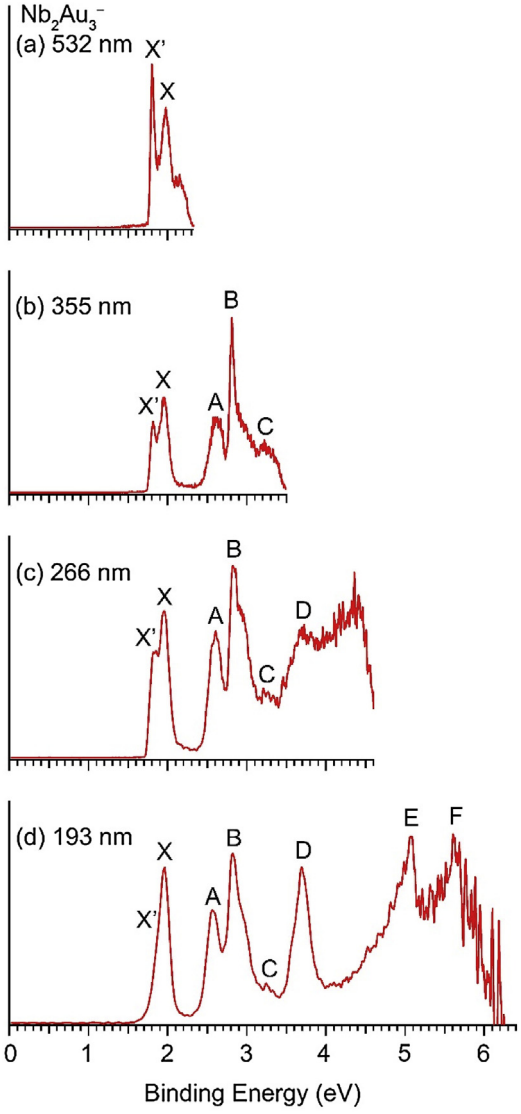

Fig. 2. Photoelectron spectra of $Nb_2Au_3^-$ at (a) 532 nm, (b) 355 nm, (c) 266 nm, and (d) 193 nm.

probably due to the increased detachment cross sections for these two bands at the higher photon energies. The 266 nm spectrum (Fig. 1c) reveals three more congested bands (F, G, H) at the high binding energy range. The 193 nm spectrum (Fig. 1d) reveals three intense and well-resolved peaks (I, J, K) and more congested features beyond peak K (L and M).

The 532 nm spectrum of $Nb_2Au_3^-$ (Fig. 2a) exhibits two sharp bands X' and X, observed at 1.81 eV and 1.96 eV, respectively. At 355 nm (Fig. 2b), three more bands (A, B, C) are observed. There is a discernible shoulder observed around 2.9 eV on the high binding energy side of band B (not labeled), which can also be seen clearly in the higher photon energy spectra. At 266 nm (Fig. 2c), the high binding energy side shows highly congested features. A broad band can be seen (labeled D), but it is much better defined in the 193 nm spectrum (Fig. 2d). At 193 nm, a large energy gap is observed following band D, beyond which two more broad features (E and F) are observed. The strong signals between 4 and 4.5 eV in the 266 nm spectrum (Fig. 2c) are not present in the 193 nm (Fig. 2d). These signals that overlap with band D could be due to a threshold enhancement at 266 nm. It will be shown below from the comparison between experiment and theory that the first sharp peak X' is from a different isomer.

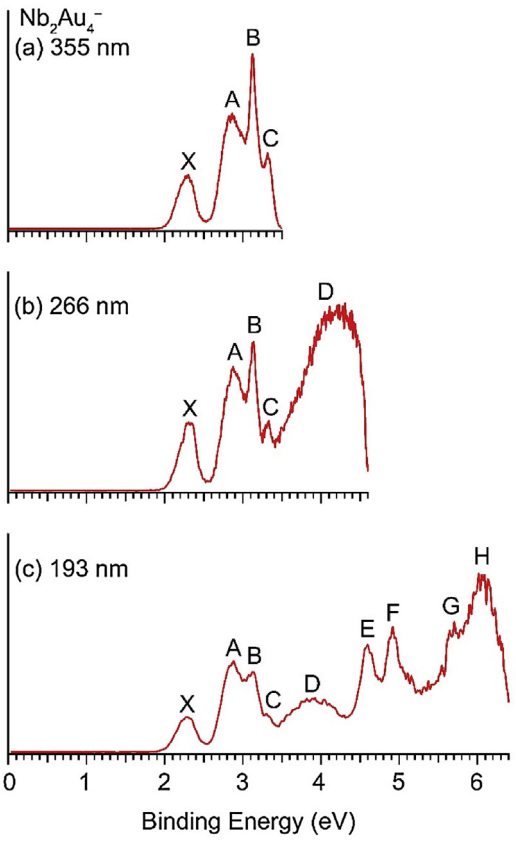

Fig. 3. Photoelectron spectra of $Nb_2Au_4^-$ at (a) 355 nm, (b) 266 nm, and (c) 193 nm.

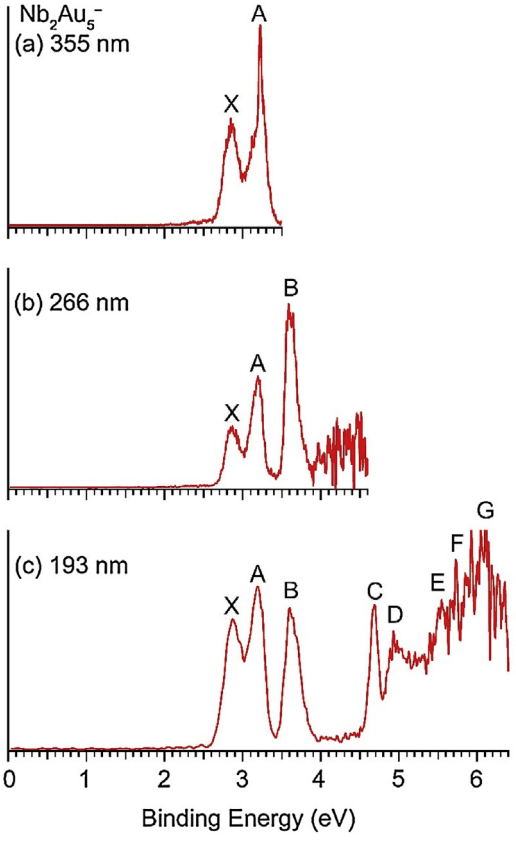

Fig. 4. Photoelectron spectra of $Nb_2Au_5^-$ at (a) 355 nm, (b) 266 nm, and (c) 193 nm.

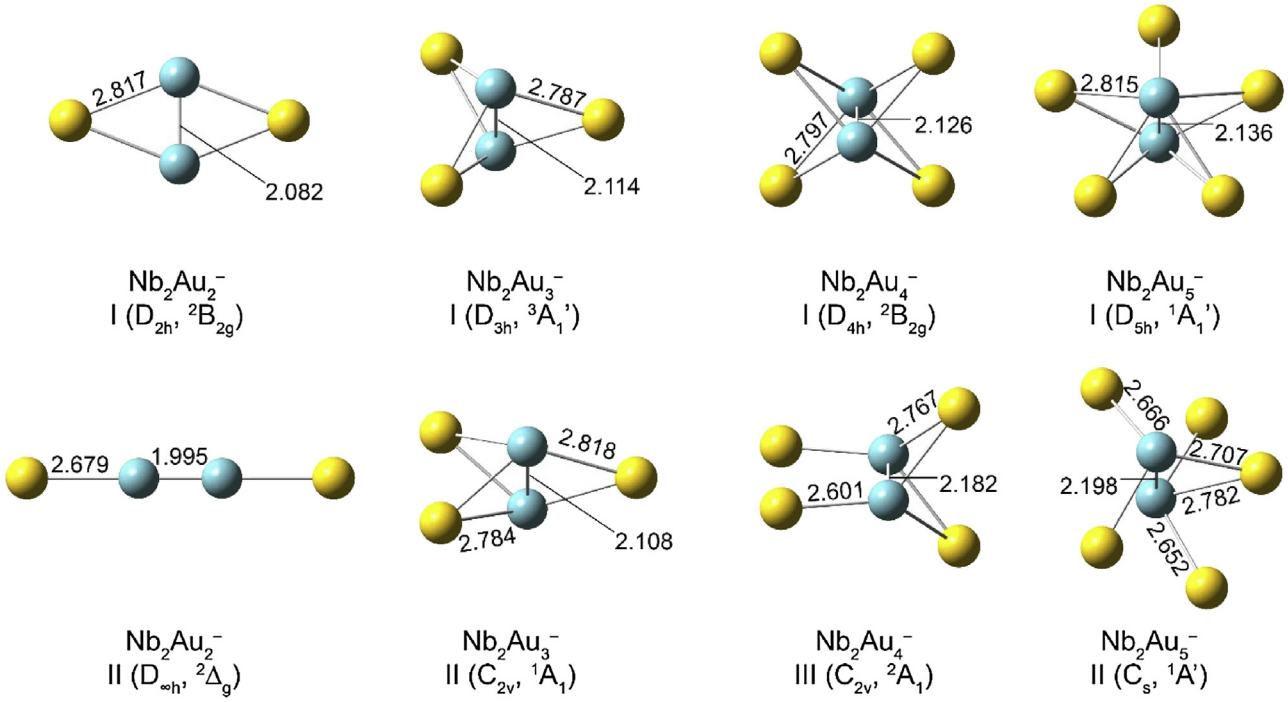

Fig. 5. The two lowest-lying isomers for $Nb_2Au_x^-$ ($x = 2-5$) at the PW91/Def2-TZVPPD level of theory. The bond lengths are given in Å.

The 355 nm spectrum (Fig. 3a) of $Nb_2Au_4^-$ displays four bands (X, A, B, C). Bands X (VDE: 2.29 eV) and A (VDE: 2.87 eV) are well separated, but quite broad, indicating there may be large geometry changes upon electron detachments or overlapping detachment transitions. Band X seems to exhibit a tail in the lower binding energy side, suggesting possible contributions from a low-lying isomer. Bands B and C are relatively sharp. At 266 nm (Fig. 3b), strong and continuous signals are observed above 3.5 eV, which are likely due to the overlap of multiple detachment transitions. At 193 nm (Fig. 3c), two relatively sharp bands (E and F) are observed, in addition to the congested features around 6 eV (G and H).

The 355 nm spectrum (Fig. 4a) of $Nb_2Au_5^-$ displays two well resolved bands, X and A, with VDEs of 2.86 eV and 3.19 eV, respectively. The 266 nm spectrum (Fig. 4b) reveals an intense band B with a VDE of 3.60 eV. Following a relatively large energy gap, numerous features are observed in the 193 nm spectrum (Fig. 4c), including a sharp band C at 4.68 eV A broad band D is observed with a VDE of 4.93 eV, beyond which the spectrum is very congested. Three more bands (E, F, G) are labeled for the sake of discussion.

4. Theoretical results

The two lowest-lying structures of each cluster at the PW91 level are presented in Fig. 5. More low-lying structures for $Nb_2Au_x^-$ ($x = 2$–5) are given in Figs. S1-S4 in the supporting information.

As shown in Fig. 5, the lowest-lying structure I for $Nb_2Au_2^-$ is found to be a rhombus with a doublet electronic state ($^2B_{2g}$) and D_{2h} symmetry. The two Au atoms are coordinated to a Nb_2 dimer in the same plane. The Nb—Nb bond length (2.082 Å) is rather short. A linear structure II ($D_{\infty h}$, $^2\Delta_g$) is 0.27 eV higher at the PW91 theory (Fig. S1). At the PBE0 level, these two structures are found to be almost degenerate with the linear structure being only 0.009 eV higher. Other low-lying isomers are at least 0.49 eV higher in energy at the PW91 level (Fig. S1).

The lowest-lying structure I of $Nb_2Au_3^-$ is found to be open-shell with a triplet ground state ($^3A_1$') and D_{3h} symmetry (Fig. 5). The next low-lying isomer II is closed-shell with C_{2v} ($^1A_1$) symmetry, which is only 0.01 eV higher at the PW91 level. At the PBE0 level, the energy of isomer II is higher than isomer I by 0.05 eV. These two structures should be considered as degenerate–both can be viewed as adding a Au atom to the D_{2h} structure of $Nb_2Au_2^-$ equatorially.

The lowest-lying structure I of $Nb_2Au_4^-$ at the PW91 level is found to be a $^2B_{2g}$ ground state with D_{4h} symmetry (Fig. 5). As shown in Fig. S3, isomer II (C_{2v}, $^2B_1$) is optimized to isomer I at the PW91 level, while it is 0.0003 eV more stable than isomer I at the PBE0 level. Since the optimized structures of isomers I and II are almost identical at PBE0 level, we believe isomer II being more stable at the PBE0 level is likely a computational artifact. The next low-lying isomer III (C_{2v}, $^2A_1$) is 0.07 eV and 0.10 eV higher than isomer I at the PW91 and PBE0 levels, respectively. Other isomers are at least 0.65 eV higher in energy at the PW91 level (Fig. S3). Isomer I of $Nb_2Au_4^-$ can be viewed simply by coordinating one more Au atom equatorially to the Nb_2 dimer of the global minimum of $Nb_2Au_3^-$.

The lowest-lying structure I of $Nb_2Au_5^-$ is found to be closed-shell with a $^1A_1$' ground state and D_{5h} symmetry. The next low-lying isomer II (C_s, $^1A'$) is 0.09 eV higher at the PW91 level, and it is optimized to isomer I at the PBE0 level. Other low-lying structures are at least 0.1 eV higher in energy. The D_{5h} structure of $Nb_2Au_5^-$ can be viewed as simply adding a Au atom equatorially to the D_{4h} structure of $Nb_2Au_4^-$.

5. Comparison between experiment and theory

The two lowest-lying isomers at the PW91 level for each cluster are considered to be the best candidates for the global minimum structure in each case. The simulated spectra, obtained by fitting a unit-area Gaussian function of 0.03 eV width to each computed VDE, are compared with the 193 nm photoelectron spectra in Figs. 6–9 for $Nb_2Au_x^-$ ($x = 2-5$), respectively. The calculated first VDEs of the two lowest-lying isomers are compared with the experimental first VDEs of $Nb_2Au_x^-$ ($x = 2$–5) in Table 2.

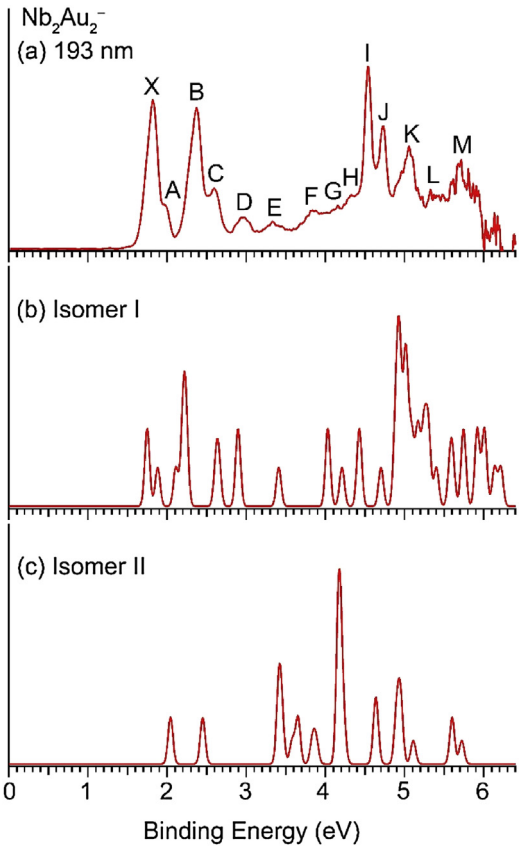

Fig. 6. Comparison between the 193 nm photoelectron spectrum of $Nb_2Au_2^-$ and the simulated spectra of the two lowest-lying isomers at the PW91 level.

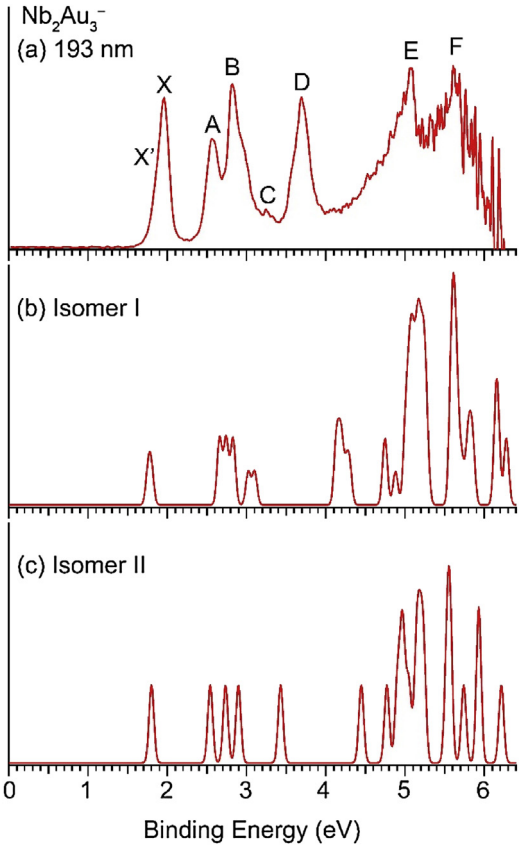

Fig. 7. Comparison between the 193 nm photoelectron spectrum of $Nb_2Au_3^-$ and the simulated spectra of the two lowest-lying isomers at the PW91 level.

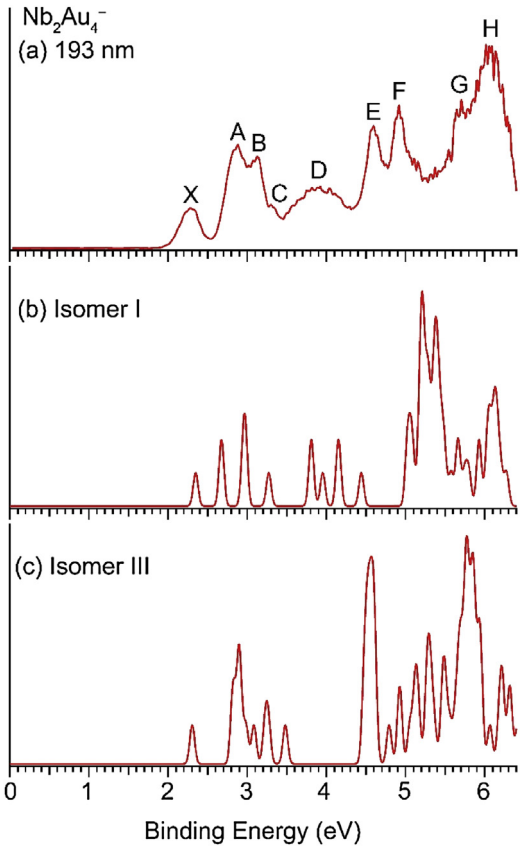

Fig. 8. Comparison between the 193 nm photoelectron spectrum of $Nb_2Au_4^-$ and the simulated spectra of the two lowest-lying isomers at the PW91 level.

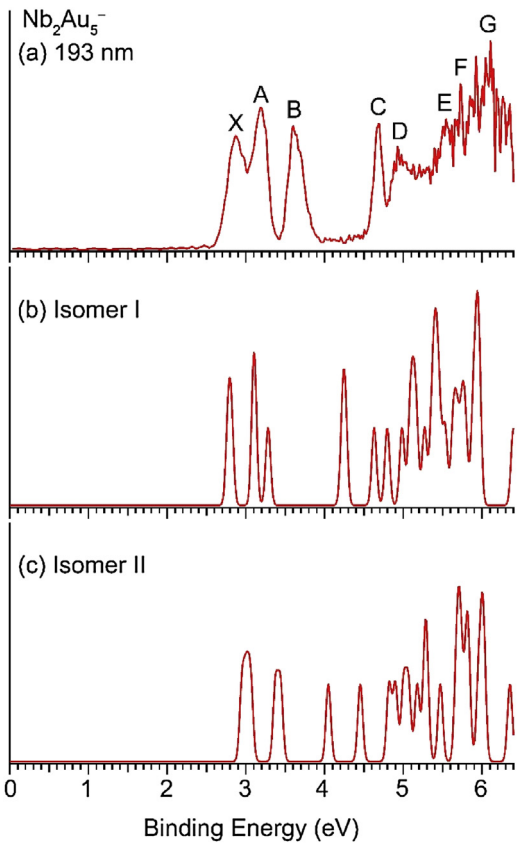

Fig. 9. Comparison between the 193 nm photoelectron spectrum of $Nb_2Au_5^-$ and the simulated spectra of the two lowest-lying isomers at the PW91 level.

Table 2
Comparison between the calculated first VDEs of the two lowest-lying isomers of $Nb_2Au_x^-$ (x = 2–5) at the PW91/Def2-TZVPPD level and the experimental first VDEs. All energies are in eV[a].

	Band	VDE (exp.)	Isomer	VDE (theo.)
$Nb_2Au_2^-$	X	1.82(2)	I	1.75
			II	2.04
$Nb_2Au_3^-$	X'	1.81(2)	I	1.76
	X	1.96(2)	II	1.80
$Nb_2Au_4^-$	X	2.29(3)	I	2.35
			III	2.30
$Nb_2Au_5^-$	X	2.86(3)	I	2.78
			II	2.95

[a] Numbers in parentheses represent the uncertainty in the last digit.

5.1. $Nb_2Au_2^-$

The simulated spectra of the top two isomers of $Nb_2Au_2^-$ are compared with the 193 nm spectrum in Fig. 6. The simulated spectrum for isomer I (Fig. 6b) is in good agreement with the experimental spectrum. The calculated first VDE is 1.75 eV, slightly lower than the experimental first VDE of 1.82 eV (Table 2). The calculated higher VDEs are consistent with the observed VDEs at high binding energies almost quantitatively in terms of the spectral pattern. The good agreement between the simulated spectrum of isomer I and the experimental data lends credence to the D_{2h} structure as the global minimum for $Nb_2Au_2^-$.

The simulated spectrum of the linear isomer II is shown in Fig. 6c, which clearly does not agree with the experimental spectrum. The calculated first VDE for isomer II is 2.04 eV, significantly higher than the experimental value of 1.82 eV (Table 2). At the PBE0 level, isomer II is almost degenerate with isomer I (Fig. S1), but at the PW91 level isomer II is 0.27 eV higher than isomer I. More importantly, there is no identifiable feature in the experimental spectra that can be attributed to isomer II. Hence, while we cannot rule out the presence of isomer II experimentally, its contribution is expected to be negligible.

5.2. $Nb_2Au_3^-$

The simulated spectra of the top two isomers of $Nb_2Au_3^-$ are compared with the 193 nm spectrum in Fig. 7. These two structures are found to be nearly degenerate at both the PW91 and PBE0 levels of theory. The computed first VDEs of the two isomers, 1.76 eV for I and 1.80 eV for II are close to each other and are found to be in reasonable agreement with the VDEs of bands X' (1.81 eV) and X (1.96 eV), respectively. Hence, bother isomers I and II probably co-exist experimentally and contribute to the experimental spectra. We can tentatively assign the observed features to different isomers by comparison with the simulated spectra. The simulated spectrum of isomer I (Fig. 7b) can reproduce qualitatively peaks X', B, C, E and F, while the simulated spectrum of isomer II can reproduce peaks X, A, B, D, E and F. The good agreement between the experimental data and the combined features from isomers I and II confirms the co-existence of both isomers experimentally and their near-degeneracy energetically. Isomers I and II of $Nb_2Au_3^-$ (Fig. 5) are very similar to each other structurally. Isomer II, being a singlet state (C_{2v}, $^1A_1$) can be viewed as originated from isomer I (D_{3h}, $^3A_1$'), due to symmetry-breaking, analogous to Jahn-Teller distortions.

5.3. $Nb_2Au_4^-$

The simulated spectra of the top two isomers (I and III in Fig. 5) of $Nb_2Au_4^-$ are compared with the experimental spectrum in Fig. 8. The calculated first VDEs of these two isomers, 2.35 eV for I and 2.30 eV for III (Table 2), are very close to each other; both are consistent with the experimental first VDE of 2.29 eV. Isomer III lies

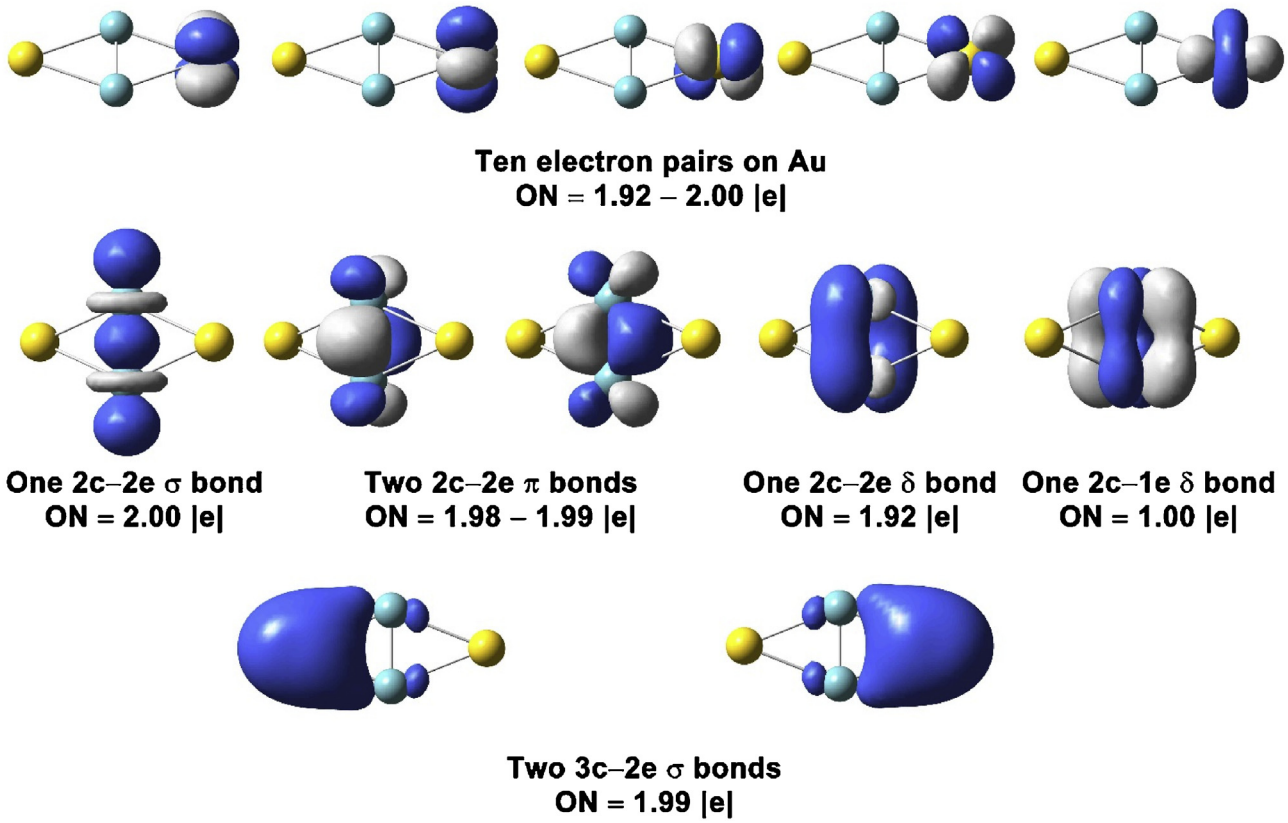

Fig. 10. Chemical bonding analyses of isomer I of $Nb_2Au_2^-$ using AdNDP.

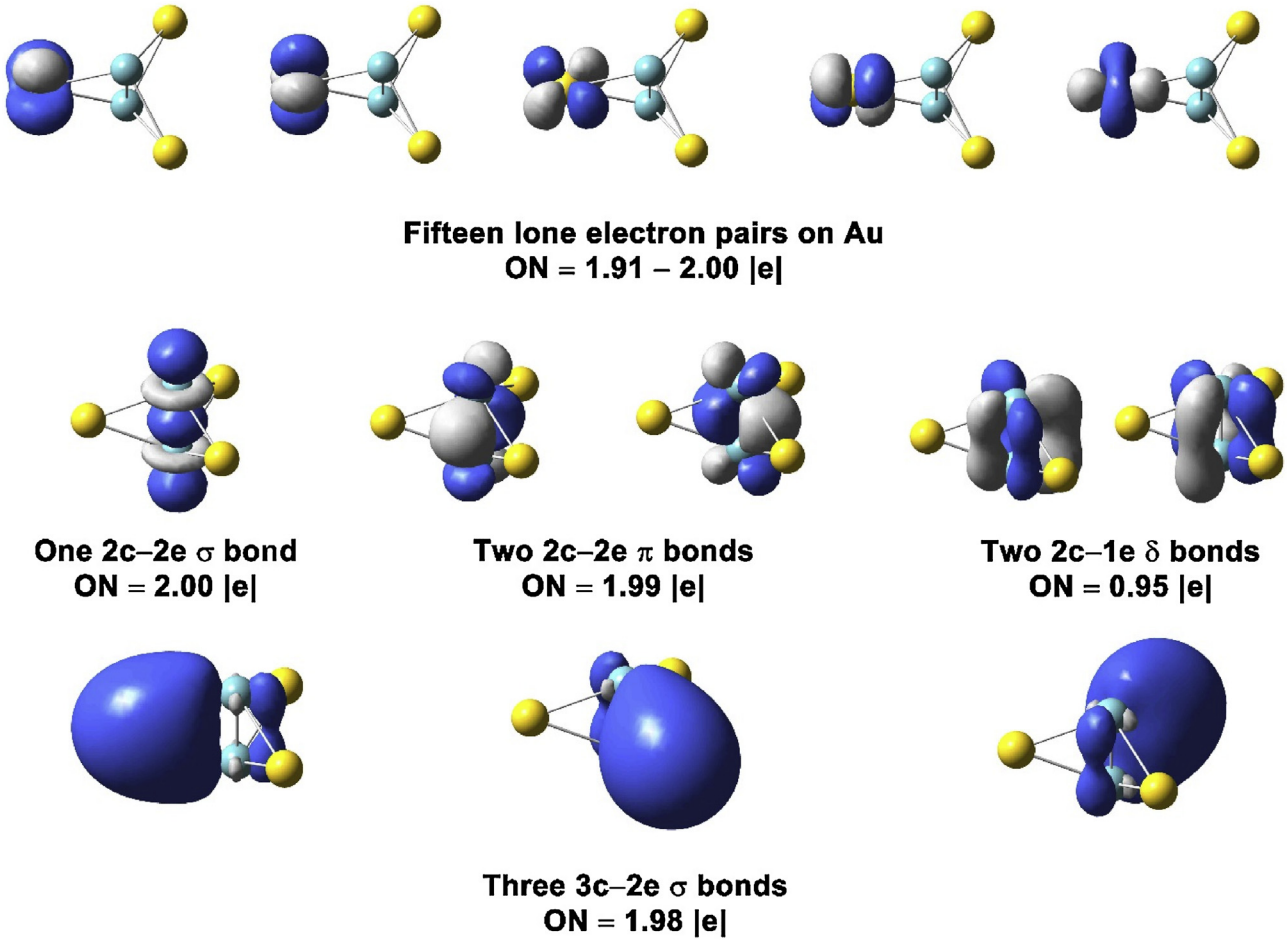

Fig. 11. Chemical bonding analyses of isomer I of $Nb_2Au_3^-$ using AdNDP.

only 0.07 eV and 0.10 eV higher in energy than isomer I at the PW91 and PBE0 levels, respectively, and is expected to be populated experimentally. The simulated spectrum of isomer I (Fig. 8b) agrees well with the observed features except band E, whereas the simulated spectrum of isomer III (Fig. 8c) can account for most features except bands D and F. Hence, both isomers are needed to interpret the experimental data, confirming that both should be present experimentally. The spectral features of $Nb_2Au_4^-$ are all quite broad (Fig. 3), partly due to the fact that many of the features of the two isomers overlap.

5.4. $Nb_2Au_5^-$

The simulated spectra of the top two isomers of $Nb_2Au_5^-$ are compared with the experimental spectrum in Fig. 9. The simulated spectral pattern of isomer I (Fig. 9b) is in qualitative agreement with the experimental spectrum. All the observed features can be identified from the simulated spectrum of isomer I. The closest low-lying isomer II is 0.09 eV higher than isomer I in energy at the PW91 level, but it is optimized to isomer I at the PBE0 level. Furthermore, the simulated spectrum of isomer II does not agree with the experimental spectrum. The well-resolved spectral features for $Nb_2Au_5^-$ (Fig. 4) do not provide evidence of contributions from minor isomers. Hence, we conclude that the D_{5h} $Nb_2Au_5^-$ isomer should be the global minimum and is the only isomer present experimentally.

6. Chemical bonding analyses

Chemical bonding in the global minima of the $Nb_2Au_x^-$ (x = 2–5) clusters is analyzed using the AdNDP method at the PW91/Def2-TZVPPD level, as shown in Figs. 10–13, respectively. The bonding in all the clusters are similar, featuring multiple bonds between the two Nb atoms and 3-center 2-electron (3c-2e) delocalized bond between each equatorial Au atom and the Nb_2 dimer, as well as five 5*d* lone pairs on each Au atom. The only difference in the bonding among the $Nb_2Au_x^-$ clusters is the bond order in the Nb_2 moiety, which decreases with increasing number of Au atoms.

In $Nb_2Au_2^-$ (Fig. 10), we find, for the bonding in the Nb_2 moiety, a 2c-2e σ bond due to the overlap of the $4d_z2$ orbitals of Nb, two 2c-2e π bonds due to the overlap of $4d_{xz}$ and $4d_{yz}$ orbitals of Nb, a 2c-2e δ bond (ON = 1.92 |e|), and a 2c-1e δ bond (ON = 1.00 |e|) involving the overlap of $4d_x2\text{-}_y2$ and $4d_{xy}$ orbitals of Nb. Thus, the formal bond order of Nb_2 in $Nb_2Au_2^-$ is 4½, consistent with the extremely short Nb – Nb bond length (2.082 Å in Fig. 5), which is comparable to that of bare Nb_2 dimer [66].

In $Nb_2Au_3^-$ (Fig. 11), the Nb—Nb bonding involves one 2c-2e σ bond, two 2c-2e π bonds, and two 2c-1e δ bonds, giving rise to a formal bond order of 4. One 2c-1e δ bond is lost sequentially in $Nb_2Au_4^-$ (Fig. 12) and $Nb_2Au_5^-$ (Fig. 13), resulting in a formal order of 3½ and 3, respectively. The decreasing bonder order in the Nb_2 moiety with x in $Nb_2Au_x^-$ is consistent with the increasing Nb—Nb bond lengths (Fig. 5). The formal bond orders in the Nb_2 moiety in $Nb_2Au_x^-$ are also consistent with the Mayer bond order analysis (Table S1). Because the Au – Nb_2 3c-2e bond consists of one electron from the 6 s orbital on Au and one electron from Nb_2, the addition of

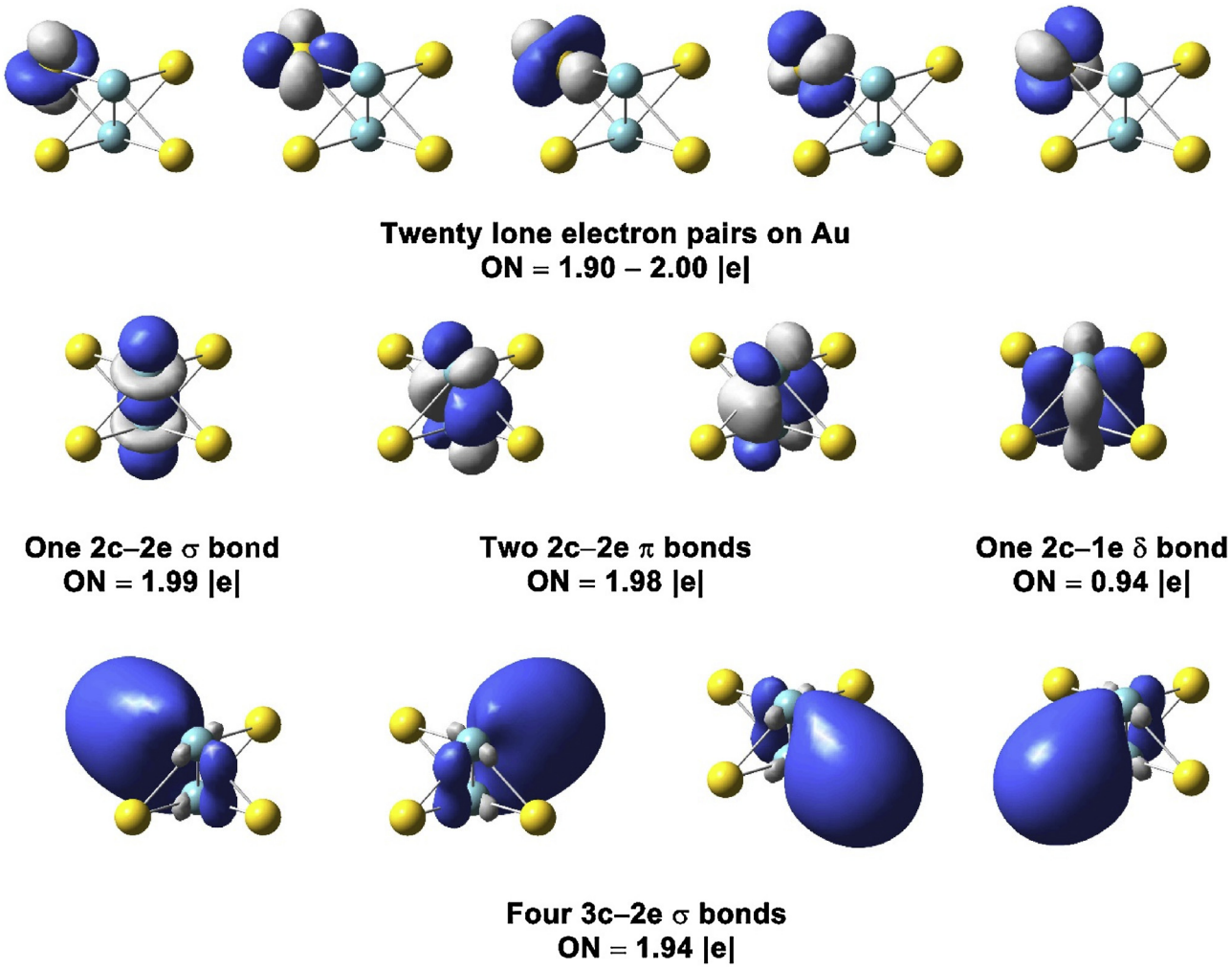

Fig. 12. Chemical bonding analyses of isomer I of $Nb_2Au_4^-$ using AdNDP.

a Au atom in $Nb_2Au_x^-$ will decrease the number of weakly bonding electrons in the Nb_2 moiety, hence its decreasing bond order with increasing x. The formal bond order of Nb_2 in $Nb_2Au_5^-$ is 3. However, the Mayer bond order analysis (Table S1) suggests a bond order for Nb_2 in $Nb_2Au_5^-$ to be larger than 3. The Nb—Nb bond length (2.136 Å) in $Nb_2Au_5^-$ is also shorter than that computed using Pyykko's triple bond radius for Nb (2×1.16 Å = 2.32 Å) [67]. This result reflects the contributions of the Au—Nb_2 3c-2e bonds to the Nb – Nb bonding, as can be glimpsed from the five 3c-2e bonds in Fig. 13.

7. Structural evolution in the $Nb_2Au_x^-$ clusters

The structures of the $Nb_2Au_x^-$ (x = 2–5) clusters, dominated by the strong Nb—Nb multiple bond, are quite unique and intriguing. The Au atoms can be viewed as special bidentate ligands coordinating to the Nb—Nb dimer equatorially and sequentially. This mode of bonding is possible, mainly due to the strong Au—Nb_2 3c-2e delocalized σ bond. This σ bond not only involves the Au6*s* orbital, but also involves weak Au5*d*-Nb4*d* interactions, as a result of the strong relativistic effects in Au. It is interesting that there is no Au—Au interaction for x = 2–5 due to the high symmetry of each cluster and the large Au—Au distance. Clearly, optimal Au—Nb_2 3-center bonding is more important than any Au—Au bonding in these clusters. As shown previously [47], the six Au atoms in $Nb_2Au_6^-$ form a six-member ring with strong Au—Au interactions, rather than six Au—Nb_2 3c-2e bonds. This mode of bonding in $Nb_2Au_6^-$ is possible for two reasons 1) the Au—Au distance is optimal, 2) the strong Nb—Nb bonding becomes more important than Au—Nb_2 bonding, because six separate Au—Nb_2 3e-2c bonds would weaken the Nb—Nb bond by breaking a strong π bond. Recently, Lu et al. have reported a joint PES and DFT study on a series of di-niobium silicon clusters, $Nb_2Si_n^-$ (n = 2–12), which were all found to contain a Nb—Nb moiety coordinated by the Si atoms [68]. There are two significant differences between the di-niobium gold and di-niobium silicon systems. In $Nb_2Si_n^-$, the Nb—Nb bond is much weaker with the Nb—Nb bond lengths ranging from 2.37 to 2.57 Å. Furthermore, all the $Nb_2Si_n^-$ clusters are characterized by strong Si – Si interactions. We expect that the equatorial coordination by Au atoms should be possible for all early 4*d* and 5*d* transition metals with strong M—M bonding in the $M_2Au_x^-$ clusters, which constitute of a unique class of bimetallic clusters and may be accessible synthetically if appropriate ligands can be designed.

8. Conclusions

Combined photoelectron spectroscopy and density functional calculations are employed to probe the structures and bonding of a series of di-niobium-doped gold clusters $Nb_2Au_x^-$ ($x = 2-5$). Global minimum searches combined with density functional calculations reveal symmetric bipyramidal type of structures for all the clusters, which can be viewed as a multiply-bonded Nb—Nb dimer coor-

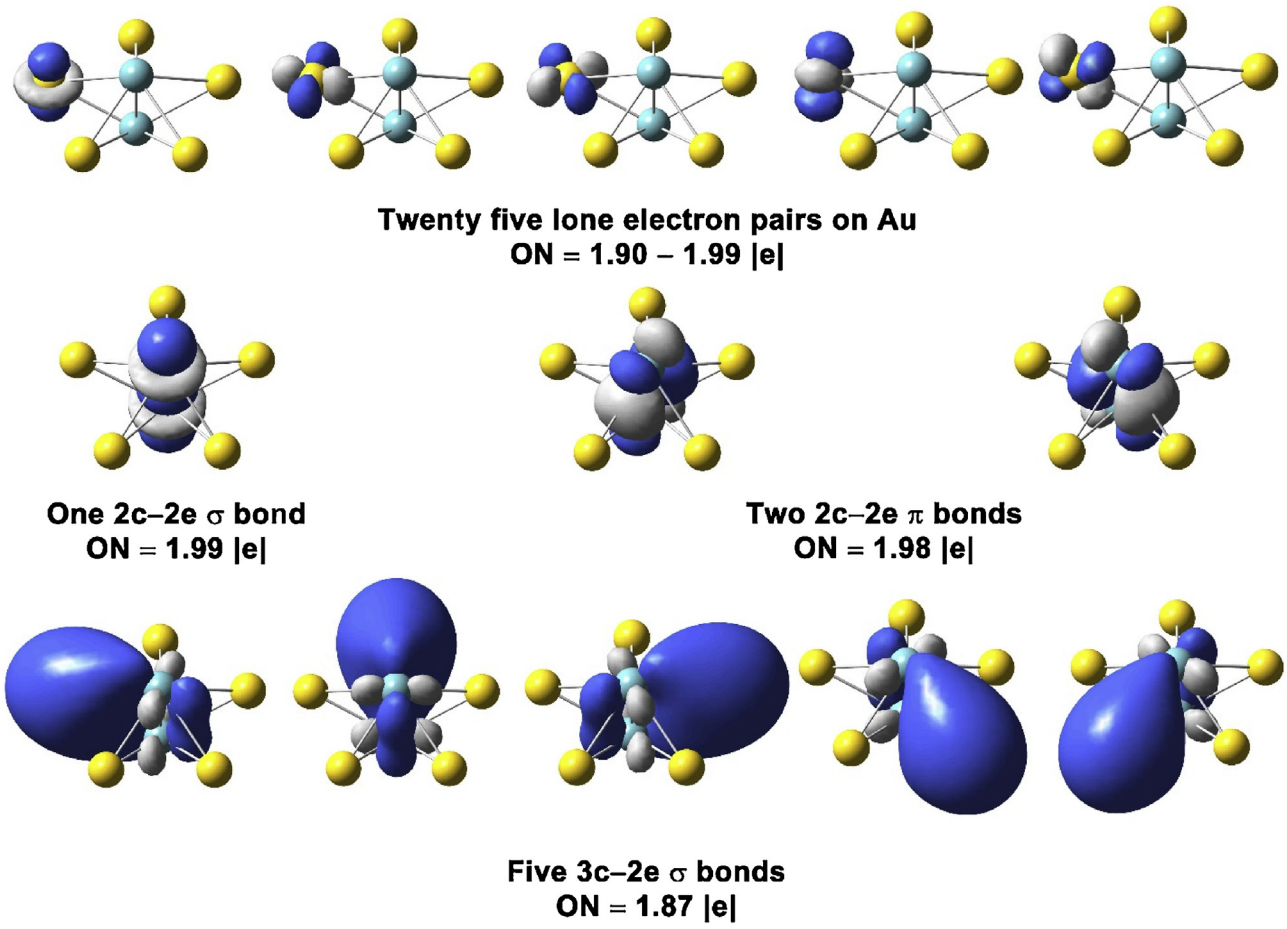

Fig. 13. Chemical bonding analyses of isomer I of $Nb_2Au_5^-$ using AdNDP.

dinated by Au atoms equatorially, resulting in highly symmetric D_{xh} structures for $x = 2–5$, respectively. Chemical bonding analyses show that there is multiple bonding between the two Nb atoms. Each Au atom forms a three-center two-electron delocalized σ bonds with the Nb_2 dimer, whereas there is little Au—Au interaction. The Nb—Nb bond length increases and the Nb—Nb bonder order decreases, as the gold atoms increases in $Nb_2Au_x^-$ ($x = 2–5$). This is a unique class of bimetallic clusters and may exist for other early transition metal $M_2Au_x^-$ type of systems.

Acknowledgments

This work was supported by the National Science Foundation (CHE-1763380). The calculations were performed using resources at the Center for Computation and Visualization (CCV) of Brown University.

Appendix A. Supplementary data

Supplementary material related to this article can be found, in the online version, at doi:https://doi.org/10.1016/j.ijms.2018.08.013.

References

[1] P. Pyykkö, Relativistic effects in structural chemistry, Chem. Rev. 88 (1998) 563–594.
[2] H. Schwarz, Relativistic effects in gas-phase ion chemistry: an experimentalist's view, Angew. Chem. Int. Ed. 42 (2003) 4442–4454.
[3] P. Pyykkö, Theoretical chemistry of gold, Angew. Chem. Int. Ed. 43 (2004) 4412–4456.
[4] P. Pyykkö, Theoretical chemistry of gold. III, Chem. Soc. Rev. 37 (2008) 1967–1997.
[5] H. Schmidbaur, A. Schier, Aurophilic interactions as a subject of current research: an up-date, Chem. Soc. Rev. 41 (2012) 370–412.
[6] A. Sommer, Alloys of gold with alkali metals, Nature 152 (1943), 215-215.
[7] A. Pantelouris, G. Kuper, J. Hormes, C. Feldmann, M. Jansen, Anionic gold in Cs_3AuO and Rb_3AuO established by x-ray absorption spectroscopy, J. Am. Chem. Soc. 117 (1995) 11749–11753.
[8] X.B. Wang, Y.L. Wang, J. Yang, X.P. Xing, J. Li, L.S. Wang, Evidence of significant covalent bonding in $Au(CN)_2-$, J. Am. Chem. Soc. 131 (2009) 16368–16370.
[9] L.S. Wang, Covalent gold, Phys. Chem. Chem. Phys. 12 (2010) 8694–8705.
[10] H.T. Liu, X.G. Xiong, P.D. Dau, Y.L. Wang, J. Li, L.S. Wang, The mixed cyanide halide Au(I) complexes, [XAuCN]– (X = F, Cl, Br, and I): evolution from ionic to covalent bonding, Chem. Sci. 2 (2011) 2101–2108.
[11] B. Kiran, X. Li, H.J. Zhai, L.F. Cui, L.S. Wang, $SiAu_4$: aurosilane, Angew. Chem. Int. Ed. 43 (2004) 2125–2129.
[12] X. Li, B. Kiran, L.S. Wang, Gold as hydrogen. An experimental and theoretical study of the structures and bonding in di-silicon gold clusters Si_2Au_n- and Si_2Au_n ($n = 2$ and 4) and comparisons to Si_2H_2 and Si_2H_4, J. Phys. Chem. A 109 (2005) 4366–4374.
[13] B. Kiran, X. Li, H.J. Zhai, L.S. Wang, Gold as hydrogen. Structural and electronic properties and chemical bonding in $Si_3Au_3+/0/-$ and comparisons to $Si_3H_3+/0/-$, J. Chem. Phys. 125 (2006), 133204.
[14] T.K. Ghanty, Gold behaves as hydrogen: prediction on the existence of a new class of boron-containing radicals, AuBX (X = F, Cl, Br), J. Chem. Phys. 123 (2005), 241101.
[15] C. Majumder, A.K. Kandalam, P. Jena, Structure and bonding of Au_5M (M = Na, Mg, Al, Si, P, S) clusters, Phys. Rev. B 74 (2006), 205437.
[16] F. Naumkin, Nano-jewellery: C_5Au_{12} – a gold-plated diamond at molecular level, Phys. Chem. Chem. Phys. 8 (2006) 2539–2545.
[17] P. Zaleski-Ejgierd, P. Pyykko, Bonding analysis for sterically uncongested simple aurocarbons C_nAu_m, Can. J. Chem. 87 (2009) 798–801.
[18] Y. Cao, C. van der Linde, R.F. Hochendorf, M.K. Beyer, The $[Au_n, Si]^-$, $n = 1–4$, potential energy surface: composition between Au—Si and Au—Au bonding, J. Chem. Phys. 132 (2010), 224307.
[19] T. Zhao, Y. Li, Q. Wang, P. Jena, All-metal clusters that mimic the chemistry of halogens, ChemPhysChem 14 (2013) 3227–3232.

[20] Y. Li, J.T. Lyon, A.P. Woodjam, P. Lievens, A. Fielicke, E. Janssens, Structural identification of gold-doped silicon clusters via far-infrared spectroscopy, J. Phys. Chem. C 119 (2006) 10896–10903.

[21] E.M. Dore, J.T. Lyon, The structures of silicon clusters doped with two gold atoms, Si_nAu_2 (n = 1–10), J. Clust. Sci. 27 (2016) 1365–1381.

[22] S.J. Lu, X.L. Xu, G. Feng, H.G. Xu, W.J. Zheng, Structural and electronic properties of $AuSi_n^-$ (n = 4–12) clusters: photoelectron spectroscopy and ab initio calculations, J. Phys. Chem. C 120 (2016) 25628–25637.

[23] H.J. Zhai, L.S. Wang, D.Y. Zubarev, A.I. Boldyrev, Gold apes hydrogen. The structure and bonding in the planar B_7Au_2– and B_7Au_2 clusters, J. Phys. Chem. A 110 (2006) 1689–1693.

[24] D.Y. Zubarev, J. Li, L.S. Wang, A.I. Boldyrev, Golden deltahedral boranes $B_xAu_x^{2-}$ (x = 5–12), Inorg. Chem. 45 (2006) 5269–5271.

[25] H.J. Zhai, C.Q. Miao, S.D. Li, L.S. Wang, On the analogy of B-BO and B-Au chemical bonding in the $B_{11}O$– and $B_{10}Au$– clusters, J. Phys. Chem. A 114 (2010) 12155–12161.

[26] Q. Chen, H. Bai, H.J. Zhai, S.D. Li, L.S. Wang, Photoelectron spectroscopy of boron-gold alloy clusters and boron boronyl clusters: B_3Au_n– and $B_3(BO)_n$– (n = 1, 2), J. Chem. Phys. 139 (2013), 044308.

[27] H. Bai, H.J. Zhai, S.D. Li, L.S. Wang, Photoelectron spectroscopy of aromatic compound clusters of the B_{12} all-boron benzene: $B_{12}Au$– and $B_{12}(BO)$–, Phys. Chem. Chem. Phys. 15 (2013) 9646–9653.

[28] Q. Chen, H.J. Zhai, S.D. Li, L.S. Wang, On the structures and bonding in boron-gold alloy clusters: B_6Au_n– and B_6Au_n (n = 1—3), J. Chem. Phys. 138 (2013), 084306.

[29] T. Jian, G.V. Lopez, L.S. Wang, Photoelectron spectroscopy of BiAu– and BiBO–: further evidence of the analogy between Au and Boronyl, J. Phys. Chem. B 120 (2016) 1635–1640.

[30] H.T. Liu, X.G. Xiong, P.D. Dau, Y.L. Wang, D.L. Huang, J. Li, L.S. Wang, Probing the nature of gold–carbon bonding in gold–alkynyl complexes, Nat. Commun. 4 (2013) 2223.

[31] I. Leon, Z. Yang, L.S. Wang, Probing the electronic structure and Au—C chemical bonding in AuC_2– and AuC_2 using high-resolution photoelectron spectroscopy, J. Chem. Phys. 140 (2014), 084303.

[32] I. Leon, F. Ruiperez, J. Ugalde, L.S. Wang, Probing the electronic structure and Au–C chemical bonding in AuC_n– and AuC_nH– (n = 2, 4, 6) using high-resolution photoelectron spectroscopy, J. Chem. Phys. 145 (2016), 064304.

[33] P. Wang, W. Zhang, X.L. Xu, J. Yuan, H.G. Xu, W.J. Zheng, Gas phase anion photoelectron spectroscopy and theoretical investigation of gold acetylide species, J. Chem. Phys. 146 (2017), 194303.

[34] I. Leon, F. Ruiperez, J.M. Ugalde, L.S. Wang, Probing the structure and chemical bonding of auropolyynes, Au-$(C{\equiv}C)_n$-Au– (n = 1–3), using high-resolution photoelectron spectroscopy, J. Chem. Phys., in press.

[35] H.G. Raubenheimer, H. Schmidbaur, Gold chemistry guided by the isolobality concept, Organometallics 31 (2012) 2507–2522.

[36] L. Gagliardi, When does gold behave as a hydrogen? Predicted uranium tetraauride and other MAu_4 tetrahedral species (M = Ti, Zr, Hf, Th), J. Am. Chem. Soc. 125 (2003) 7504–7505.

[37] Y. Erdogdu, T. Jian, G.V. Lopez, W.L. Li, L.S. Wang, On the electronic structure and chemical bonding of titanium tetraauride: $TiAu_4$ and $TiAu_4^-$, Chem. Phys. Lett. 610/611 (2014) 23–28.

[38] L. Gagliardi, P. Pyykko, Study of the MAu6 (M = Cr, Mo, W) molecular species: a transition from halogenlike to hydrogenlike chemical behavior for gold, Phys. Chem. Chem. Phys. 6 (2004) 2904–2906.

[39] X. Li, B. Kiran, L.F. Cui, L.S. Wang, Magnetic properties in transition metal doped gold clusters: $M@Au_6$ (M = Ti, V, Cr), Phys. Rev. Lett. 95 (2005), 253401.

[40] L. Lin, T. Holtzl, P. Gruene, P. Claes, G. Meijer, A. Fielicke, P. Lievens, M.T. Nguyen, Fluxionality and aromaticity in small yttrium-doped gold clusters, ChemPhysChem 9 (2008) 2471–2474.

[41] M. Zhang, L.M. He, L.X. Zhao, X.J. Feng, Y.H. Luo, Tuning magnetic moments by 3d transition-metal-doped Au_6 clusters, J. Phys. Chem. C 113 (2009) 6491–6496.

[42] L. Lin, P. Claes, T. Holtzl, E. Jansseens, T. Wende, R. Bergmann, G. Santambrogio, G. Meijer, K.R. Asmis, M.T. Nguyen, P. Lievens, The structure of Au_6Y^+ in the gas phase, Phys. Chem. Chem. Phys. 12 (2010) 13907–13913.

[43] L. Lin, P. Claes, P. Gruene, G. Meijer, A. Fielicke, M.T. Nguyen, P. Lievens, Far-infrared spectra of yttrium-doped gold clusters Au_nY (n = 1-9), ChemPhysChem 11 (2010) 1932–1943.

[44] P.V. Nhat, M.T. Nguyen, Trends in structural, electronic and energetic properties of bimetallic vanadium-gold clusters Au_nV with n = 1-14, Phys. Chem. Chem. Phys. 13 (2011) 16254–16264.

[45] J. Jung, H. Kim, J.C. Kim, M.H. Park, Y.K. Han, Gold behaves as hydrogen in the intermolecular self-interaction of metal auride MAu_4 (M = Ti, Zr, Hf), Chem. Asian J. 6 (2011) 868–872.

[46] D. Dong, Z. Ben-Xia, W. Hui, D. Quan, Geometries, stabilities, and magnetic properties of Au_nTi (n = 1–9) clusters, A density functional study, Compt. Theor. Chem. 1025 (2013) 67–73.

[47] T. Jian, L.F. Cheung, J. Czekner, T.T. Chen, G.V. Lopez, W.L. Li, L.S. Wang, Chem. Sci. 8 (2017) 7528–7536.

[48] B. Wang, L. Xie, X.J. Liu, W.J. Chen, Y.F. Zhang, X. Huang, Structural evolution and chemical bonding of diniobium boride clusters $Nb_2B_x^{-/\circ}$ (x = 1–6): hexagonal-bipyramidal $Nb_2B_6^{-/0}$ species, Eur. J. Inorg. Chem. (2018) 940–950.

[49] L.S. Wang, H.S. Cheng, J. Fan, Photoelectron spectroscopy of size-selected transition metal clusters: Fe_n^-, n = 3–24, J. Chem. Phys. 102 (1995) 9480–9493.

[50] L.S. Wang, Photoelectron spectroscopy of size-selected boron clusters: from planar structures to borophenes and borospherenes, Int. Rev. Phys. Chem. 35 (2016) 69–142.

[51] S. Kirkpatrick, C.D. Gelatt, M.P. Vecchi, Optimization by simulated annealing, Science 220 (1983) 671–680.

[52] S.T. Call, D.Y. Zubarev, A.I. Boldyrev, Global minimum structure searches via particle swarm optimization, J. Comput. Chem. 28 (2007) 1177–1186.

[53] J.P. Perdew, Y. Wang, Pair-distribution function and its coupling-constant average for the spin-polarized electron gas, Phys. Rev. B 46 (1992) 12947–12953.

[54] P.J. Hay, W.R. Wadt, Ab initio effective core potentials for molecular calculations. Potentials for K to Au including the outermost core orbitals, J. Chem. Phys. 82 (1985) 299–310.

[55] J.P. Perdew, K. Burke, M. Ernzerhof, Generalized gradient approximation made simple, Phys. Rev. Lett. 77 (1996) 3865–3868.

[56] C. Adamo, V. Barone, Toward reliable density functional methods without adjustable parameters: The PBE0 model, J. Chem. Phys. 110 (1999) 6158–6170.

[57] F. Weigend, R. Ahlrichs, Balanced basis sets of split valence, triple zeta valence and quadruple zeta valence quality for H to Rn: design and assessment of accuracy, Phys. Chem. Chem. Phys. 7 (2005) 3297–3305.

[58] D. Rappoport, F. Furche, Property-optimized Gaussian basis sets for molecular response calculations, J. Chem. Phys. 133 (2010), 134105.

[59] D. Figgen, G. Rauhut, Dolg M, H. Stoll, Energy-consistent pseudopotentials for group 11 and 12 atoms: adjustment to multi-configuration Dirac–Hartree–Fock data, Chem. Phys. 311 (2005) 227–244.

[60] K.A. Peterson, D. Figgen, M. Dolg, H. Stoll, Energy-consistent relativistic pseudopotentials and correlation consistent basis sets for the 4d elements Y–Pd, J. Chem. Phys. 126 (2007), 124101.

[61] M.E. Casida, C. Jamorski, K.C. Casida, D.R. Salahub, Molecular excitation energies to high-lying bound states from time-dependent density-functional response theory: characterization and correction of the time-dependent local density approximation ionization threshold, J. Chem. Phys. 108 (1998) 4439–4449.

[62] D.Y. Zubarev, A.I. Boldyrev, Developing paradigms of chemical bonding: adaptive natural density partitioning, Phys. Chem. Chem. Phys. 10 (2008) 5207–5217.

[63] D.Y. Zubarev, B.B. Averkiev, H.J. Zhai, L.S. Wang, A.I. Boldyrev, Aromaticity and antiaromaticity in transition-metal systems, Phys. Chem. Chem. Phys. 10 (2008) 257–267.

[64] R. Dennington, T. Keith, J.M. Millam, GaussView, Version 4.1, Semichem. Inc., Shawnee Mission, KS, 2007.

[65] M.J. Frisch, G.W. Trucks, H.B. Schlegel, G.E. Scuseria, M.A. Robb, J.R. Cheeseman, G. Scalmani, V. Barone, B. Mennucci, G.A. Petersson, H. Nakatsuji, M. Caricato, X. Li, H.P. Hratchian, A.F. Izmaylov, J. Bloino, G. Zheng, J.L. Sonnenberg, M. Hada, M. Ehara, K. Toyota, R. Fukuda, J. Asegawa, M. Ishida, T. Nakajima, Y. Honda, O. Kitao, H. Nakai, T. Vreven, J.A. Montgomery Jr, J.E. Peralta, F. Ogliaro, M. Bearpark, J.J. Heyd, E. Brothers, K.N. Kudin, V.N. Staroverov, R. Kobayashi, J. Normand, K. Raghavachari, A. Rendell, J.C. Burant, S.S. Iyengar, J. Omasi, M. Cossi, N. Rega, J.M. Millam, M. Klene, J.E. Knox, J.B. Cross, V. Bakken, C. Adamo, J. Jaramillo, R. Gomperts, R.E. Stratmann, O. Yazyev, A.J. Austin, R. Cammi, C. Pomelli, J.W. Ochterski, R.L. Martin, K. Morokuma, V.G. Zakrzewski, G.A. Voth, P. Salvador, J.J. Dannenberg, S. Dapprich, A.D. Daniels, Ö. Farkas, J.B. Foresman, J.V. Ortiz, J. Cioslowski, D.J. Fox, Gaussian 09, Revision C.01, Gaussian, Inc, Wallingford, CT, 2009.

[66] A.M. James, P. Kowalczyk, R. Fournier, B. Simard, Electronic spectroscopy of the niobium dimer molecule: experimental and theoretical results, J. Chem. Phys. 99 (1993) 8504–8518.

[67] P. Pyykko, Additive covalent radii for single-, double-, and triple-bonded molecules and tetrahedrally bonded crystals: a summary, J. Phys. Chem. A 119 (2015) 2326–2337.

[68] S.J. Lu, H.G. Xu, X.L. Xu, W.J. Zheng, Anion photoelectron spectroscopy and theoretical investigation on $Nb_2Si_n^{-/0}$ (n = 2-12) clusters, J. Phys. Chem. C 121 (2017) 11851–11861.